International Forum on Aeroelasticity and Structural Dynamics
IFASD 2017
25-28 June 2017 Como, Italy

SEMI-ANALYTICAL UNSTEADY AERODYNAMIC MODELING FOR A FLEXIBLE THIN AIRFOIL IN ARBITRARY MOTION

Cristina Riso[1], Giorgio Riccardi[2,3], and Franco Mastroddi[1]

[1]Department of Mechanical and Aerospace Engineering
Sapienza University of Rome
via Eudossiana, 18 Roma 00184 Italy
cristina.riso@uniroma1.it

[2]Department of Mathematics and Physics
University of Campania "Luigi Vanvitelli"
viale A. Lincoln, 5 Caserta 81100, Italy

[3]National Research Council of Italy
Maritime Research Center (CNR-INSEAN)
via di Vallerano, 139 Rome 00128, Italy

Keywords: Unsteady Aerodynamics, Flexible Airfoils, Discrete-Vortex Method, Free Wake.

Abstract: A semi-analytical formulation for the unsteady aerodynamics of flat plates is extended to flexible thin airfoils. The velocity field is described by means of a complex potential, which is developed by mapping the airfoil boundary onto a circle. This well-established approach adopted in several small disturbance theories is generalized to airfoil motions of arbitrary amplitude, under the only assumptions of attached flow and constant body length. Vorticity shedding from the airfoil trailing edge is modeled using a discrete-vortex method to account for non-planar wake. A semi-analytical solution for the pressure jump on the body is obtained that may be used for parametric studies and assessment of high-fidelity solvers. Numerical results are presented for a cantilevered flexible airfoil undergoing imposed motion in a steady axial flow.

1 INTRODUCTION

Two-dimensional incompressible potential-flow unsteady aerodynamics plays a key role in aeroelasticity since the beginning of the past century. The relative physics simplicity and availability of sound theoretical approaches have allowed to obtain several closed-form solutions for the aerodynamic load on moving airfoils [1–8]. Despite great progresses in computational fluid dynamics and experimental methods, such theoretical models are still used as low-order simulation tools and for validation of high-fidelity solvers.

Recent research on theoretical modeling of unsteady aerodynamics is driven by the interest in applications such as bioinspired unmanned aerial vehicles, morphing airfoils, and fluttering devices for energy harvesting [9–11]. Indeed, there is a need of analytical models to preliminarily investigate the aeroelastic effects of large-amplitude motion and body deformation before performing high-fidelity computations or experimental campaigns. Benchmarks for assessment of fully numerical models are also necessary. Traditional theoretical solutions may not be suitable

for these purposes since they are valid only for small disturbances and flat wake [1–8]. Therefore, large-amplitude flat-plate models have been recently developed [12–15]. However, there is still a lack of general modeling approaches to simultaneously take into account large-amplitude motion, body flexibility, and free-wake effects in a unique theory.

This paper presents a semi-analytical formulation for the unsteady aerodynamics of flexible thin airfoils that generalizes the flat-plate model presented and validated in Ref. [16]. The velocity field is described by means of a complex potential [17], which is evaluated by mapping the airfoil boundary onto a circle [18]. This well-established approach traditionally adopted to derive small disturbance theories [3] is here generalized to study airfoil rigid-body motion and deformation of arbitrary amplitude, under the only assumptions of attached flow and constant body length. Vorticity shedding from the trailing edge is modeled using a discrete-vortex method [19] to account for non-planar wake. A semi-analytical solution for the pressure jump on the airfoil is obtained that simultaneously includes large-amplitude motion, body flexibility, and free-wake effects. Numerical results for a cantilevered flexible airfoil undergoing imposed motion in a steady axial flow are presented to show the capabilities of the proposed model.

The paper is organized as follows. A generalized map for flexible thin airfoils in arbitrary motion is introduced in Sec. 2. The complex potential is developed in Sec. 3. The pressure jump on the body is obtained in Sec. 4. Numerical results are presented in Sec. 5. Concluding remarks and future work are discussed in Sec. 6.

2 GENERALIZED MAPPING

The present formulation is based on the standard hypotheses of inviscid and incompressible fluid in attached, planar, and irrotational flow, which allow to develop a theoretical model via complex analysis [17, 18]. The physical plane of the flow is identified with the complex plane, and an auxiliary plane is also introduced. The position vectors in the two planes are identified with the complex variables $\boldsymbol{x}$ and $\boldsymbol{\omega}$, respectively. The velocity field around a flexible thin airfoil in the $\boldsymbol{x}$-plane is described in terms of a complex potential [17], which is developed in the $\boldsymbol{\omega}$-plane by mapping the airfoil boundary onto a circle [18]. To this purpose, the time-dependent map used to develop the flat-plate model in Ref. [16] is here generalized to account for body deformation. As main advantage, using a time-dependent transformation that follows the moving airfoil boundary allows to study rigid-body and elastic motions of arbitrary amplitude, under the only assumptions of attached flow and constant body length. Conversely, standard time-constant maps [18] transform the airfoil boundary in its reference configuration and are thus suitable to study only small disturbances [3, 5, 8]. A body-fixed reference frame is frequently introduced to model large-amplitude rigid-body motion still using a stationary map [13, 15], but this approach is not applicable to study large airfoil deformations.

2.1 Geometry and kinematics

The present unsteady aerodynamic model is developed by introducing the following time-dependent map from the $\boldsymbol{\omega}$-plane to the $\boldsymbol{x}$-plane

$$\boldsymbol{x}(\boldsymbol{\omega};t) = \boldsymbol{h}(t) + \frac{\ell\,\overline{\boldsymbol{\chi}}(t)}{4}\,\sum_{k=1}^{n}\,\boldsymbol{c}_k(t)\,\left(\boldsymbol{\omega}^k + \boldsymbol{\omega}^{-k}\right) \tag{1}$$

This is assumed smooth in both $\boldsymbol{\omega}$ and t, with $\partial_{\boldsymbol{\omega}}\boldsymbol{x} \neq 0$ at any point on the unit circle $\mathcal{C}$ apart from the points $\boldsymbol{\omega} = \pm 1$.

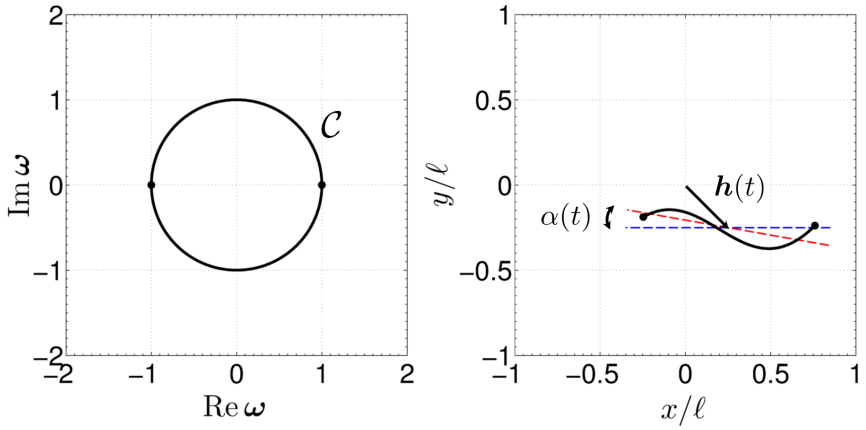

Figure 1: Unit circle in the $\boldsymbol{\omega}$-plane (left) mapped onto a curved thin airfoil in the $\boldsymbol{x}$-plane (right) by means of Eq. (1) for $n = 3$, $\ell = 1$, $\boldsymbol{h} = 0.25 - \boldsymbol{i}0.25$, $\alpha = 10°$, $\boldsymbol{c}_1 = 1$, $\boldsymbol{c}_2 = \boldsymbol{i}0.075$, $\boldsymbol{c}_3 = \boldsymbol{i}0.125$. Coordinates are normalized by the circle radius (left) and by the airfoil length (right).

The map in Eq. (1) transforms points on $\mathcal{C}$ in the $\boldsymbol{\omega}$-plane into points on the boundary of a thin airfoil undergoing rigid-body motion and deformation in the $\boldsymbol{x}$-plane (see the example in Fig. 1). No assumption is placed on the motion amplitude, provided that the flow remains attached and that the body undeformed length ℓ is conserved. Arbitrary rigid-body translation is taken into account in Eq. (1) by the function $\boldsymbol{h}(t) = h_x(t) + \boldsymbol{i}h_y(t)$, which gives the instantaneous position of the undeformed airfoil centroid. The function $\overline{\boldsymbol{\chi}}(t) := \exp[-\boldsymbol{i}\alpha(t)]$ introduces a rigid-body rotation by the instantaneous clockwise-positive angle of attack $\alpha(t)$. The body deformed shape is described by the complex coefficients $\boldsymbol{c}_k(t) = c_k^r(t) + \boldsymbol{i}c_k^i(t)$ $(k = 1, 2, \ldots, n)$, n being the order of the truncated Laurent series [18] in Eq. (1). The transformation used in Ref. [16] to model a flat plate is a special case of Eq. (1) obtained by taking $n = 1$ and $\boldsymbol{c}_1(t) \equiv 1$. If $n > 1$ Laurent coefficients are used, the transformation in Eq. (1) describes a deformed thin airfoil with $n - 2$ curvature sign changes along the chord.

The body boundary is obtained from Eq. (1) for $\boldsymbol{\omega} \in \mathcal{C}$, namely by taking $\boldsymbol{\omega} = \exp(\boldsymbol{i}\theta)$ with $\theta \in [0, 2\pi)$:

$$\boldsymbol{x}_b(\theta; t) := \boldsymbol{x}(e^{\boldsymbol{i}\theta}; t) = \boldsymbol{h}(t) + \frac{\ell\,\overline{\boldsymbol{\chi}}(t)}{2} \sum_{k=1}^{n} \boldsymbol{c}_k(t)\, \cos k\theta \tag{2}$$

The upper and lower sides are spanned for $\theta \in [0, \pi)$ and $\theta \in [\pi, 2\pi)$, respectively. Cosine functions are only present in Eq. (2) for the zero-thickness condition.

Having assumed the angle θ in Eq. (2) as Lagrangian parameter, the velocity $\boldsymbol{u}_b$ of a generic point on the airfoil boundary is evaluated as

$$\boldsymbol{u}_b(\theta; t) := \partial_t \boldsymbol{x}_b(\theta; t) = \dot{\boldsymbol{h}}(t) + \frac{\ell\,\overline{\boldsymbol{\chi}}(t)}{2} \sum_{k=1}^{n} \left[\dot{\boldsymbol{c}}_k(t) - \boldsymbol{i}\,\dot{\alpha}(t)\,\boldsymbol{c}_k(t)\right] \cos k\theta \tag{3}$$

Note that the angle θ could more generally be a function of time in Eq. (2). Indeed, different choices of the parametrization of the airfoil boundary give body velocities that differ only for a tangent contribution, which does not influence the surrounding flow in an inviscid model.

2.2 Critical points

The critical points of the map [Eq. (1)] are the points of the $\boldsymbol{x}$-plane obtained by mapping the zeros of $\partial_{\boldsymbol{\omega}}\boldsymbol{x}$ in the $\boldsymbol{\omega}$-plane. The location of these points and their role in the present unsteady aerodynamic model is discussed below.

The $\boldsymbol{\omega}$-derivative of Eq. (1) can be written as $\partial_{\boldsymbol{\omega}}\boldsymbol{x} = \boldsymbol{Q}_{2n}/\boldsymbol{\omega}^{n+1}$ where

$$\boldsymbol{Q}_{2n}(\boldsymbol{\omega};t) = \frac{\ell\,\overline{\boldsymbol{\chi}}(t)}{4}\,\boldsymbol{\omega}^n \sum_{k=1}^{n} k\,\boldsymbol{c}_k(t)\,\left(\boldsymbol{\omega}^k - \boldsymbol{\omega}^{-k}\right) \tag{4}$$

$$= \frac{\ell\,\overline{\boldsymbol{\chi}}(t)}{4}\,(\boldsymbol{\omega}^2-1) \sum_{k=1}^{n} k\,\boldsymbol{c}_k(t)\,\boldsymbol{\omega}^{n-k}\,\left(\boldsymbol{\omega}^{2k-2} + \boldsymbol{\omega}^{2k-4} + \ldots + \boldsymbol{\omega}^2 + 1\right) \tag{5}$$

is a time-dependent polynomial of degree $2n$ in $\boldsymbol{\omega}$. The zeros of $\partial_{\boldsymbol{\omega}}\boldsymbol{x}$ are the $2n$ zeros of $\boldsymbol{Q}_{2n}$.

Equation (4) shows that the points $\boldsymbol{\omega} = \pm 1$ on $\mathcal{C}$ are zeros of $\boldsymbol{Q}_{2n}$ for any value of n. These points are mapped through Eq. (1) onto the airfoil leading and trailing edges, which are thus critical points of the map for any body deformed shape. Since $\partial_{\boldsymbol{\omega}}\boldsymbol{x}$ is assumed non zero at any point $\boldsymbol{\omega} \neq \pm 1$ on $\mathcal{C}$ (see Subsec. 2.1), the airfoil edges are the only critical points on the body boundary.

Equation (5) and the property $\boldsymbol{x}(\boldsymbol{\omega}) = \boldsymbol{x}(1/\boldsymbol{\omega})$ of Eq. (1) show that if a generic point $\boldsymbol{\omega} \neq 0$ is a zero of $\boldsymbol{Q}_{2n}$ then $1/\boldsymbol{\omega}$ is also a zero. The other $2n-2$ zeros of $\boldsymbol{Q}_{2n}$ are thus $n-1$ inside $\mathcal{C}$ and $n-1$ outside $\mathcal{C}$. The latter are denoted by $\boldsymbol{\Lambda}_m(t)$ $(m = 1, 2, \ldots, n-1)$ and are mapped onto $n-1$ critical points $\boldsymbol{Y}_m(t)$ in the fluid domain by Eq. (1). As well known for flat-plate airfoils, points inside $\mathcal{C}$ are not mapped onto the same Riemann surface as those outside $\mathcal{C}$ [18]. For this reason, the points inside $\mathcal{C}$ are not considered when mapping the $\boldsymbol{\omega}$-plane onto the $\boldsymbol{x}$-plane. Therefore, the $n-1$ zeros of $\boldsymbol{Q}_{2n}$ inside $\mathcal{C}$ do not give critical points in the fluid domain.

The critical points of the map in Eq. (1) are branch points, namely origins of branch cuts [18]. Since the airfoil edges are critical points for any value of n, the body boundary is always branch cut for the map, as well known in the case of a flat plate [16]. Equation (1) involves powers of $\boldsymbol{\omega}$ and $1/\boldsymbol{\omega}$ higher than the first one when describing curved bodies $(n > 1)$. Since this give $n-1$ critical points in the fluid domain as shown above, $n-1$ branch cuts are also present. The kth branch cut $\mathcal{BC}_k$ is a curve running from the critical point $\boldsymbol{Y}_k$ to infinity. Its preimage $\mathcal{BCP}_k$ in the $\boldsymbol{\omega}$-plane is an infinite curve passing through the point $\boldsymbol{\Lambda}_k$, which divides it into two parts $\mathcal{BCP}_k^{\pm}$. The branch cut positive and negative sides $\mathcal{BC}_k^{\pm}$ are introduced as the left-hand and right-hand sides of $\mathcal{BC}_k$ as moving along the curve from $\boldsymbol{Y}_k$ to infinity (see Fig. 2). The positive side $\mathcal{BC}_k^{+}$ is described by the curve $\boldsymbol{x} = \boldsymbol{x}(\boldsymbol{\omega}^+)$ with $\boldsymbol{\omega}^+ \in \mathcal{BCP}_k^{+}$, while the negative side $\mathcal{BC}_k^{-}$ by the curve $\boldsymbol{x} = \boldsymbol{x}(\boldsymbol{\omega}^-)$ with $\boldsymbol{\omega}^- \in \mathcal{BCP}_k^{-}$. The orientation of $\mathcal{BC}_k^{\pm}$ yields consistent orientations of $\mathcal{BCP}_k^{\pm}$ as shown in Fig. 2. The role of the branch cuts of Eq. (1) is further discussed in Subsec. 2.3 and 3.3.

In the present unsteady aerodynamic model the complex potential $\boldsymbol{\Phi}(\boldsymbol{x};t)$ describing the velocity field around a flexible thin airfoil in the $\boldsymbol{x}$-plane is obtained by developing the complex potential $\tilde{\boldsymbol{\Phi}}(\boldsymbol{\omega};t)$ in the $\boldsymbol{\omega}$-plane and by next mapping the $\boldsymbol{\omega}$-plane onto the $\boldsymbol{x}$-plane using Eq. (1). The conjugate velocity at any point of the $\boldsymbol{x}$-plane is thus given by [17]

$$\overline{\boldsymbol{u}}[\boldsymbol{x}(\boldsymbol{\omega};t);t] = \frac{\partial_{\boldsymbol{\omega}}\tilde{\boldsymbol{\Phi}}(\boldsymbol{\omega};t)}{\partial_{\boldsymbol{\omega}}\boldsymbol{x}(\boldsymbol{\omega};t)} \tag{6}$$

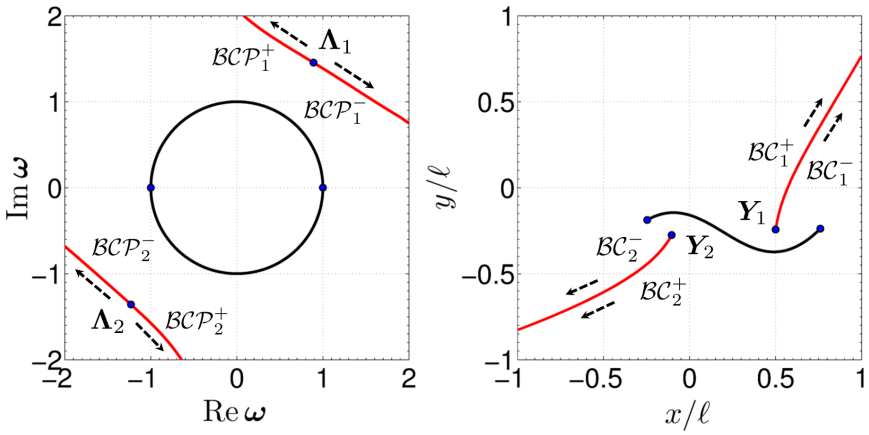

Figure 2: Critical points and branch cuts of the map in Eq. (1) (right) and their preimages (left) for the parameters in Fig. 1. Coordinates are normalized by the circle radius (left) and by the airfoil length (right).

Equation (6) is singular at the critical points of the map, since $\partial_{\boldsymbol{\omega}} \boldsymbol{x}$ vanishes at the corresponding points of the $\boldsymbol{\omega}$-plane. The velocity singularity at the airfoil leading edge is allowed, while the one at the trailing edge is removed by a Kutta condition (see Subsec. 3.2.3). The singularities at the $n-1$ critical points $\boldsymbol{Y}_m(t) = \boldsymbol{x}[\boldsymbol{\Lambda}_m(t); t]$ must be also removed since these points are in the fluid domain. The regularity of the velocity field [Eq. (6)] at the critical points $\boldsymbol{Y}_m(t)$ must be thus imposed together with to the no-penetration unsteady boundary condition and the recovery of the freestream velocity at infinity when developing the complex potential (see Sec. 3). Note that the regularity condition is not involved in the case of flat-plate airfoils, for which the only critical points of Eq. (1) are the airfoil edges [16].

2.3 Map inversion and branch cuts

In Subsec. (2.2) it has been shown that the map in Eq. (1) has $n-1$ branch cuts in the fluid domain. The consequences of this behavior on the unsteady aerodynamic model are discussed below. The discussion refers to a fixed time, so that time dependencies are omitted.

The inverse function of the map in Eq. (1) satisfies the following equation of degree $2n$:

$$\boldsymbol{\omega}^{2n} + \frac{\boldsymbol{c}_{n-1}}{\boldsymbol{c}_n}\,\boldsymbol{\omega}^{n-1} + \cdots + \frac{\boldsymbol{c}_1}{\boldsymbol{c}_n}\,\boldsymbol{\omega}^{n+1} - \frac{4\,\boldsymbol{\chi}\,(\boldsymbol{x}-\boldsymbol{h})}{\ell\,\boldsymbol{c}_n}\,\boldsymbol{\omega} + \frac{\boldsymbol{c}_1}{\boldsymbol{c}_n}\,\boldsymbol{\omega}^{n-1} + \cdots + \frac{\boldsymbol{c}_{n-1}}{\boldsymbol{c}_n}\,\boldsymbol{\omega} + 1 = 0 \quad (7)$$

having n roots inside $\mathcal{C}$ and n roots outside $\mathcal{C}$. When the map in Eq. (1) models a flat plate its inverse function is thus given by the only solution of Eq. (7) transforming points of the $\boldsymbol{x}$-plane into points outside $\mathcal{C}$ in the $\boldsymbol{\omega}$-plane. However, $n > 1$ solutions of Eq. (7) verify this property when the map in Eq. (1) describes a curved airfoil. Indeed, body curvature is introduced in the map by adding powers of $\boldsymbol{\omega}$ and $1/\boldsymbol{\omega}$ up to an order $n > 1$. The region of the $\boldsymbol{\omega}$-plane outside $\mathcal{C}$ thus consists of n distinct regions mapped by Eq. (1) onto complete complex planes on different Riemann surfaces. The region bounded by $\mathcal{C}$ and by the $n-1$ curves $\mathcal{BCP}_k$ is the preimage D of the $\boldsymbol{x}$-plane through Eq. (1) (see Fig. 3). The other $n-1$ regions (shown in red in Fig. 3) are mapped onto complex planes on different Riemann surfaces than the plane of the flow, so that points in these regions shall be not considered when transforming the $\boldsymbol{\omega}$-plane into the $\boldsymbol{x}$-plane. For a generic order $n > 1$ of the map in Eq. (1) its inverse function is thus the solution of Eq. (7) transforming points of the $\boldsymbol{x}$-plane into points of D, which in this case does not coincide with the whole region of the $\boldsymbol{\omega}$-plane outside $\mathcal{C}$.

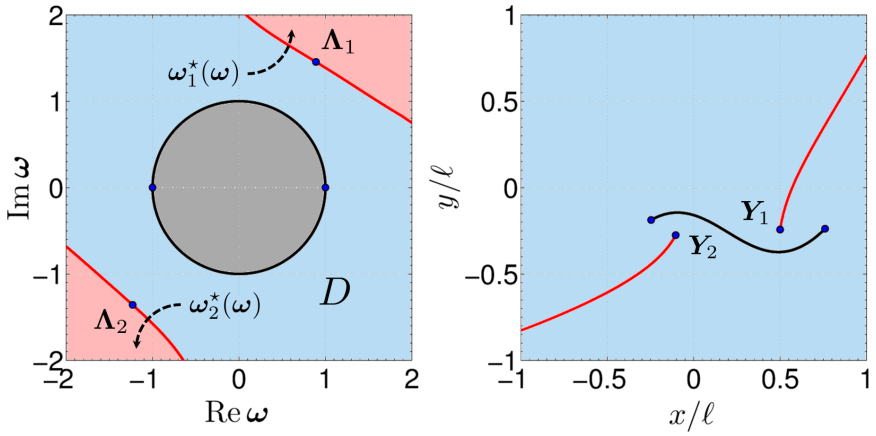

Figure 3: Action of the functions $\boldsymbol{\omega}_k^\star(\boldsymbol{\omega})$ associated to the map in Eq. (1) for the parameters in Fig. 1. Coordinates are normalized by the circle radius (left) and by the airfoil length (right).

For any point $\boldsymbol{\omega} \in D$, the other points of the $\boldsymbol{\omega}$-plane that are mapped onto the same location as $\boldsymbol{x}(\boldsymbol{\omega})$ on other Riemann surfaces are obtained by solving the equation $\boldsymbol{x}(\boldsymbol{\omega}) = \boldsymbol{x}(\boldsymbol{\omega}^\star)$ with respect to $\boldsymbol{\omega}^\star$ and by neglecting the trivial solution $\boldsymbol{\omega}^\star = \boldsymbol{\omega}$. The $n-1$ solutions outside $\mathcal{C}$ define an equal number of functions $\boldsymbol{\omega}_k^\star = \boldsymbol{\omega}_k^\star(\boldsymbol{\omega})$ $(k = 1, \ldots, n-1)$ that transform D into the $n-1$ regions outside to $\mathcal{C}$ not considered in the mapping (red regions in Fig. 3). The function $\boldsymbol{\omega}_k^\star$ verifies the property $\boldsymbol{\omega}_k^\star(\boldsymbol{\Lambda}_k) = \boldsymbol{\Lambda}_k$ and it transforms points $\boldsymbol{\omega}^+ \in \mathcal{BCP}_k^+$ into points $\boldsymbol{\omega}^- \in \mathcal{BCP}_k^-$ (and vice versa).

The consequences of the above discussion on the unsteady aerodynamic model are clarified by means of an example for the case $n = 3$. Consider a set of circles $\mathcal{C}_r$ in the $\boldsymbol{\omega}$-plane with center at the origin and increasing radius $r > 1$. Consider also the curves in the $\boldsymbol{x}$-plane obtained by mapping these circles using Eq. (1). For $1 < r \leq \Lambda_1 := |\boldsymbol{\Lambda}_1|$, the circles are transformed into simple closed curves around the airfoil as shown in Fig. 4. When $r = \Lambda_1$ the corresponding circle passes through $\boldsymbol{\Lambda}_1$, and its image in the $\boldsymbol{x}$-plane has a cusp at the critical point $\boldsymbol{Y}_1 = \boldsymbol{x}(\boldsymbol{\Lambda}_1)$ (see Figs. 4 and 5). Next, the circles become non-simple self-intersecting curves in the $\boldsymbol{x}$-plane for $\Lambda_1 < r < \Lambda_2 := |\boldsymbol{\Lambda}_2|$. This occurs because some points of these circles are located outside D, so they are mapped onto locations already obtained by previous points but on a different Riemann surface. The self-intersection $\boldsymbol{x}^\pm := \boldsymbol{x}(\boldsymbol{\omega}^\pm)$ on each mapped circle lie on the branch cut $\mathcal{BC}_1$, with $\boldsymbol{\omega}^\pm \in \mathcal{BCP}_1^\pm$ as shown in Fig. 5. The same behavior is observed for $r \geq \Lambda_2$ as shown in Fig. 6.

The above remarks can be extended to a generic order n of the map in Eq. (1), for which $n-1$ critical points $\boldsymbol{Y}_k$ and associated branch cuts $\mathcal{BC}_k$ are present in the fluid domain. As pointed out in Figure 5, crossing one of these branch cuts at a generic point $\boldsymbol{x}^\pm \neq \boldsymbol{Y}_k$ in the $\boldsymbol{x}$-plane implies skipping from the point $\boldsymbol{\omega}^+ \in \mathcal{BCP}_k^+$ to the distinct point $\boldsymbol{\omega}^- \in \mathcal{BCP}_k^-$ in the $\boldsymbol{\omega}$-plane (or vice versa). Indeed, the points of the $\boldsymbol{\omega}$-plane outside D are not considered in the mapping. As a consequence, any function of $\boldsymbol{\omega}$ different from the map itself is discontinuous across the $n-1$ curves $\mathcal{BC}_k$ once it is rewritten as a function of $\boldsymbol{x}$ using the map in Eq. (1). In particular, this behavior affects the velocity field [Eq. (6)] and shall be conveniently corrected to remove unphysical discontinuities in the fluid domain (see Subsec. 3.3).

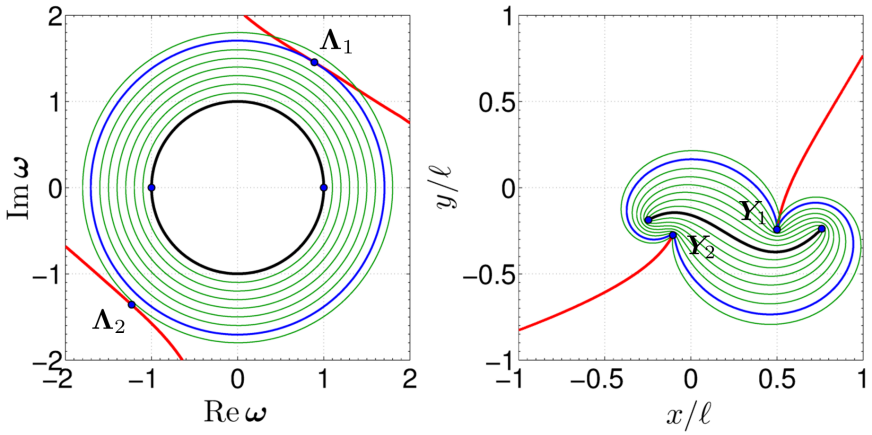

Figure 4: Circles in the $\boldsymbol{\omega}$-plane with center at the origin and increasing radius $1 < r < \rho$ with $\rho < \Lambda_2$ (left) and their images in the $\boldsymbol{x}$-plane through the map in Eq. (1) (right) for the parameters in Fig. 1. Coordinates are normalized by the circle radius (left) and by the airfoil length (right).

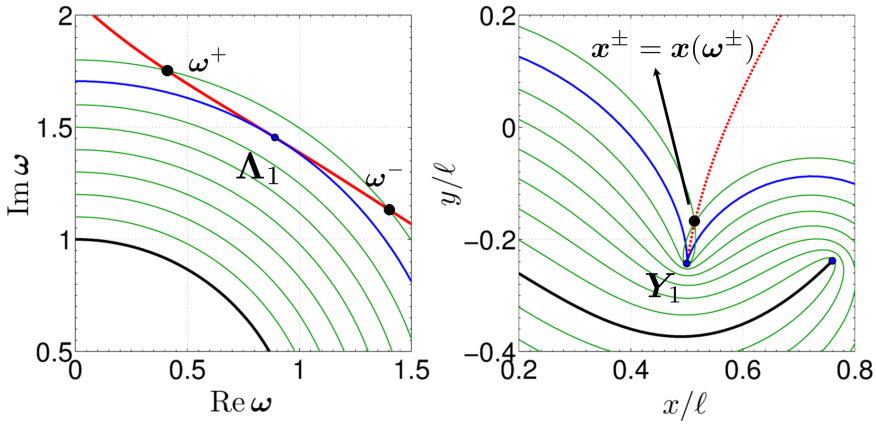

Figure 5: Zoom of Fig. 4

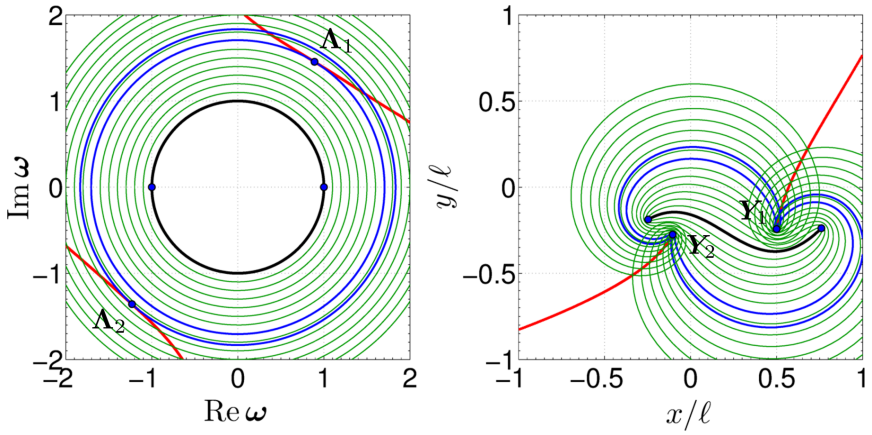

Figure 6: Circles in the $\boldsymbol{\omega}$-plane with center at the origin and increasing radius $1 < r < \rho$ with $\rho > \Lambda_2$ (left) and their images through the map in Eq. (1) (right) for the parameters in Fig. 1. Coordinates are normalized by the circle radius (left) and by the airfoil length (right).

3 COMPLEX POTENTIAL

The velocity field around a flexible thin airfoil in the $\boldsymbol{x}$-plane is modeled by developing the complex potential $\tilde{\boldsymbol{\Phi}}$ in the $\boldsymbol{\omega}$-plane and by next mapping the $\boldsymbol{\omega}$-plane onto the $\boldsymbol{x}$-plane [Eq. (1)]. The conjugate velocity in the $\boldsymbol{x}$-plane is then given by Eq. (6). Following the traditional approach [3, 5], the complex potential in the $\boldsymbol{\omega}$-plane is split in its noncirculatory and circulatory contributions as follows:

$$\tilde{\boldsymbol{\Phi}}(\boldsymbol{\omega};t) = \tilde{\boldsymbol{\Phi}}^{(nc)}(\boldsymbol{\omega};t) + \tilde{\boldsymbol{\Phi}}^{(c)}(\boldsymbol{\omega};t) \tag{8}$$

These are separately developed in Subsec. 3.1 and 3.2. Remarks on the limits of validity of the present model are given in 3.3. The flat-plate model presented and validated in Ref. [16] can be recovered as special case of the following general formulation.

3.1 Noncirculatory flow

The noncirculatory contributions in Eq. (8) are obtained by imposing: 1) the no-penetration unsteady boundary condition on the moving airfoil; 2) the recovery of the freestream velocity at infinity; and 3) the regularity of the velocity field [Eq. (6)] at the critical points of the map in the fluid domain.

3.1.1 No-penetration unsteady boundary condition

The no-penetration condition requires the normal components of the body and fluid velocities to be equal at any point on the body boundary. Once the local normal vector is written as $\boldsymbol{n}(\theta;t) = -\boldsymbol{i}\,\partial_\theta \boldsymbol{x}_b(\theta;t)$, using Eqs. (2) and (3) the normal component of the body velocity $u_{b_n} := \boldsymbol{u}_b \cdot \boldsymbol{n} = \mathrm{Re}(\overline{\boldsymbol{u}}_b\,\boldsymbol{n})$ is evaluated as

$$u_{b_n} = \frac{1}{2}\,\Big[\,\sum_{s=1}^{n} \boldsymbol{p}_s\,\left(\boldsymbol{\omega}^{+s} - \boldsymbol{\omega}^{-s}\right) + \sum_{r,j=1}^{n} \boldsymbol{q}_{r,j}\;\left(\boldsymbol{\omega}^{+r+j} + \boldsymbol{\omega}^{-r+j} - \boldsymbol{\omega}^{+r-j} - \boldsymbol{\omega}^{-r-j}\right)\Big] \tag{9}$$

where the time-dependent imaginary coefficients

$$\boldsymbol{p}_s := \frac{\ell}{4}\,s\,\left(\overline{\boldsymbol{\chi}}\,\dot{\overline{\boldsymbol{h}}}\,\boldsymbol{c}_s - \boldsymbol{\chi}\,\dot{\boldsymbol{h}}\,\overline{\boldsymbol{c}}_s\right) \qquad \boldsymbol{q}_{r,j} := \frac{\ell^2}{16}\,j\,\left[\,\left(\dot{\overline{\boldsymbol{c}}}_r\boldsymbol{c}_j - \dot{\boldsymbol{c}}_r\overline{\boldsymbol{c}}_j\right) + \boldsymbol{i}\,\dot{\alpha}\;\left(\overline{\boldsymbol{c}}_r\boldsymbol{c}_j + \boldsymbol{c}_r\overline{\boldsymbol{c}}_j\right)\,\right] \tag{10}$$

are known functions of the instantaneous body shape and kinematics.

By considering the terms in Eq. (9), the complex potential $\tilde{\boldsymbol{\Phi}}^{(nc)}(\boldsymbol{\omega};t)$ is searched as

$$\tilde{\boldsymbol{\Phi}}^{(nc)}(\boldsymbol{\omega};t) = \sum_{\substack{m=-2n \\ m\neq 0}}^{n} \boldsymbol{d}_m(t)\,\boldsymbol{\omega}^m \tag{11}$$

The lower bound of the truncated Laurent series in Eq. (11) is assumed as $-2n$ since Eq. (9) involves powers of $\boldsymbol{\omega}$ from $-2n$ up to $2n$. The upper bound is assumed equal to n as in Eq. (1) to satisfy the recovery of the freestream velocity at infinity. Substituting the derivative of Eq. (11) into Eq. (6) and writing the map derivative on the airfoil boundary as $\partial_{\boldsymbol{\omega}}\boldsymbol{x} = \boldsymbol{i}\,\boldsymbol{\omega}\,\partial_\theta \boldsymbol{x}_b$ the normal component of the fluid velocity $u_n := \boldsymbol{u}\cdot\boldsymbol{n} = \mathrm{Re}(\overline{\boldsymbol{u}}\,\boldsymbol{n})$ is obtained as

$$u_n = \frac{1}{2}\,\sum_{m=-2n}^{n} m\,\left(\boldsymbol{d}_m\,\boldsymbol{\omega}^m + \overline{\boldsymbol{d}}_m\,\boldsymbol{\omega}^{-m}\right) \tag{12}$$

The no-penetration boundary condition is satisfied by identically equating Eqs. (9) and (12). This gives the following $4n$ relations:

$$
\begin{aligned}
n+1 \le k_1 \le 2n \qquad & k_1\, \boldsymbol{d}_{-k_1} = +\sum_{m=k_1-n}^{n} \boldsymbol{q}_{m,-m+k_1} \\
1 \le k_2 \le n \qquad & k_2(\boldsymbol{d}_{k_2} - \overline{\boldsymbol{d}}_{-k_2}) = +\boldsymbol{p}_{k_2} + \sum_{m=1}^{\star k_2-1} \boldsymbol{q}_{m,-m+k_2} + \sum_{m=1}^{\star n-k_2} \boldsymbol{q}_{m,+m+k_2} - \sum_{m=k_2+1}^{\star n} \boldsymbol{q}_{m,+m-k_2} \\
-n \le k_3 \le -1 \qquad & k_3(\boldsymbol{d}_{k_3} - \overline{\boldsymbol{d}}_{-k_3}) = -\boldsymbol{p}_{-k_3} - \sum_{m=1}^{\star -k_3-1} \boldsymbol{q}_{m,-m-k_3} - \sum_{m=1}^{\star n+k_3} \boldsymbol{q}_{m,+m-k_3} + \sum_{m=-k_3+1}^{\star n} \boldsymbol{q}_{m,+m+k_3} \\
-2n \le k_4 \le -n-1 \qquad & k_4\, \boldsymbol{d}_{k_4} = -\sum_{m=-k_4-n}^{n} \boldsymbol{q}_{m,-m-k_4}
\end{aligned}
\tag{13}
$$

where the summations denoted by * are considered only if the upper bound is not smaller than the lower one. The conditions in Eq. (13) relate the $3n$ unknown coefficients of the complex potential in Eq. (11) to the known coefficients in Eq. (10). However, the fourth and third set of conditions in Eq. (13) are respectively the conjugates of the first and second one ($k_1 = -k_4$, $k_2 = -k_3$). Therefore, only $2n$ equations in Eq. (13) are independent, which are not sufficient to evaluate the $3n$ coefficients in Eq. (11).

3.1.2 Recovery of the freestream velocity at infinity

One further condition is obtained by imposing that the flow velocity asymptotically recovers its undisturbed value $\boldsymbol{u}_\infty$ for $\boldsymbol{x} \to \infty$. Since the circulatory terms in Eq. (8) give zero velocity at infinity, this condition is imposed only on the complex potential in Eq. (11). Substituting the derivatives of Eqs. (1) and (11) into Eq. (6) and imposing $\overline{\boldsymbol{u}} \to \overline{\boldsymbol{u}}_\infty$ for $\boldsymbol{\omega} \to \infty$ gives

$$
\boldsymbol{d}_n = \frac{\ell\, \overline{\boldsymbol{\chi}}}{4}\, \overline{\boldsymbol{u}}_\infty\, \boldsymbol{c}_n \tag{14}
$$

3.1.3 Regularity of the velocity field at the critical points of the map

Using Eq. (6), the conjugate velocity due to the complex potential in Eq. (11) is written as

$$
\overline{\boldsymbol{u}}^{(nc)}[\boldsymbol{x}(\boldsymbol{\omega};t);t] = \frac{1}{\boldsymbol{\omega}^n}\, \frac{\boldsymbol{P}_{3n}(\boldsymbol{\omega};t)}{\boldsymbol{Q}_{2n}(\boldsymbol{\omega};t)} \tag{15}
$$

having introduced the following time-dependent polynomial of degree $3n$ in $\boldsymbol{\omega}$:

$$
\boldsymbol{P}_{3n} := \boldsymbol{\omega}^{n+1}\, \partial_{\boldsymbol{\omega}} \tilde{\boldsymbol{\Phi}}^{(nc)} = \sum_{m=-2n}^{n} m\, \boldsymbol{d}_m\, \boldsymbol{\omega}^{m+2n} \tag{16}
$$

The conjugate velocity (15) is singular at the $n-1$ critical points of the map $\boldsymbol{Y}_m(t) = \boldsymbol{x}[\boldsymbol{\Lambda}_m(t);t]$ in the fluid domain (see Subsec. 2.2). These unphysical singularities are removed by imposing that the points $\boldsymbol{\Lambda}_m(t)$ be zeros of $\boldsymbol{P}_{3n}$ with at least the same multiplicity as for $\boldsymbol{Q}_{2n}$. In the case of distinct zeros, this gives $n-1$ equations of the form

$$
\boldsymbol{P}_{3n}[\boldsymbol{\Lambda}_m(t);t] \equiv 0 \qquad (m = 1, 2, \ldots, n-1) \tag{17}
$$

The no-penetration unsteady boundary condition, the recovery of the freestream velocity at infinity, and the regularity of the velocity field at the points $\boldsymbol{Y}_m$ result in a system of $3n$ equations [Eqs. (13), (14), and (17)] whose solution gives the unknown coefficients of the complex potential in Eq. (11) as functions of the instantaneous body shape and kinematics and of the velocity of the undisturbed flow.

3.2 Circulatory flow

The circulatory terms in Eq. (8) are due to the shed vorticity and to consequent circulation that is developed around the body (Kelvin theorem). Vorticity shedding from the airfoil trailing edge is here modeled using a discrete-vortex method in order account for free-wake effects [19]. Since the wake dynamics has to be simulated by means of a time-marching algorithm when using discrete vortices, the present unsteady aerodynamic model is not fully closed-form like linearized flat-wake theories [1–4]. However, it is applicable to large-amplitude motions while still remaining analytical in space. The well-known complex potentials of a discrete vortex and of the body circulation developed for flat-plate airfoils [17] are not valid for deformed shapes described by Eq. (1). Hence, a general formulation is developed below.

3.2.1 Complex potential of a unit-circulation vortex

Consider a vortex of unit circulation in presence of a flexible thin airfoil described by Eq. (1). The vortex is placed at a point $\boldsymbol{x}_v(t) := \boldsymbol{x}[\boldsymbol{\omega}_v(t); t]$ of the $\boldsymbol{x}$-plane, corresponding to a point $\boldsymbol{\omega}_v(t) \in D(t)$ of the $\boldsymbol{\omega}$-plane. The complex potential of the vortex is developed in the $\boldsymbol{\omega}$-plane by imposing that the vortex-induced conjugate velocity in the $\boldsymbol{x}$-plane: 1) locally behave as $1/\{2\pi\boldsymbol{i}\,[\boldsymbol{x}-\boldsymbol{x}_v]\}$ for $\boldsymbol{x}\to\boldsymbol{x}_v$; 2) asymptotically tend to $1/(2\pi\boldsymbol{i}\,\boldsymbol{x})$ for $\boldsymbol{x}\to\infty$; 3) be tangent to the body boundary; and 4) be regular at the critical points $\boldsymbol{Y}_m$.

The local behavior of the conjugate velocity (condition 1) and no-penetration (condition 3) can be satisfied by assuming the following complex potential:

$$\tilde{\boldsymbol{\Phi}}^{(v)}(\boldsymbol{\omega};t) = \frac{1}{2\pi\boldsymbol{i}}\left\{\log[\boldsymbol{\omega}-\boldsymbol{\omega}_v(t)] + \log\boldsymbol{\omega} - \log[\boldsymbol{\omega}-1/\overline{\boldsymbol{\omega}}_v(t)]\right\} \tag{18}$$

where the circle theorem [17] has been used. As well-known, the complex potential in Eq. (18) gives the velocity field due to a vortex of unit circulation outside a flat plate [17]. However, the conjugate velocity in the $\boldsymbol{x}$-plane due to Eq. (18) does not have the required asymptotic behavior (condition 2) when the map in Eq. (1) models curve body shapes. Indeed, the $\boldsymbol{\omega}$-derivative of Eq. (18) tends to $1/(2\pi\boldsymbol{i}\,\boldsymbol{\omega})$ for $\boldsymbol{\omega}\to\infty$, while from Eq. (1) one has $\partial_{\boldsymbol{\omega}}\boldsymbol{x}\to n\,\boldsymbol{x}/\boldsymbol{\omega}$ for $\boldsymbol{\omega}\to\infty$. Therefore, the vortex-induced conjugate velocity in the $\boldsymbol{x}$-plane [Eq. (6)] due to Eq. (18) behaves as $1/(2\pi\boldsymbol{i}\,n\,\boldsymbol{x})$ for $\boldsymbol{x}\to\infty$, which does not verify the condition 2 for $n>1$.

The correct asymptotic behavior of the vortex-induced velocity field can be obtained for a generic n in Eq. (1) by including further $n-1$ logarithmic terms of the form $\log[\boldsymbol{\omega}-\boldsymbol{w}_k(t)]$ in Eq. (18). The additional contributions must be regular around $\boldsymbol{x}_v$ (condition 1) and also give tangent velocities on the airfoil boundary (condition 3). These requirements can be satisfied with the choice $\boldsymbol{w}_k(t) := \boldsymbol{\omega}_k^{\star}[\boldsymbol{\omega}_v(t);t]$ $(j=1,2,\ldots,n-1)$ and using the circle theorem. Indeed, the points $\boldsymbol{w}_k(t)$ so introduced are always outside $D(t)$, and the conjugate of their reciprocals are also outside $D(t)$ since they are located inside $\mathcal{C}$ (see Subsec. 2.3). Therefore, the additional logarithmic terms and the ones obtained from the latter when using the circle theorem do not

introduce unphysical singularities in the flow field. The complex potential in Eq. (18) is thus modified in the following one:

$$\begin{aligned}\tilde{\boldsymbol{\Phi}}^{(v)}(\boldsymbol{\omega};t) \;=\; & \frac{1}{2\pi\boldsymbol{i}}\left\{\log[\boldsymbol{\omega}-\boldsymbol{\omega}_v(t)]+\log\boldsymbol{\omega}-\log[\boldsymbol{\omega}-1/\overline{\boldsymbol{\omega}}_v(t)]\right\}+\\ &+\frac{1}{2\pi\boldsymbol{i}}\sum_{k=1}^{n-1}\left\{\log[\boldsymbol{\omega}-\boldsymbol{w}_k(t)]+\log\boldsymbol{\omega}-\log[\boldsymbol{\omega}-1/\overline{\boldsymbol{w}}_k(t)]+\right.\\ &\left.+\frac{\boldsymbol{a}_k(t)}{\boldsymbol{\omega}-\boldsymbol{w}_k(t)}+\frac{\overline{\boldsymbol{a}}_k(t)/\overline{\boldsymbol{w}}_k^2(t)}{\boldsymbol{\omega}-1/\overline{\boldsymbol{w}}_k(t)}\right\}\end{aligned} \tag{19}$$

which verifies the conditions 1), 2), and 3). The regularity of the vortex-induced velocity field at the critical points $\boldsymbol{Y}_m$ (condition 4) is satisfied by evaluating the coefficients $\boldsymbol{a}_k$ $(k=1,\ldots,n-1)$ so that the $\boldsymbol{\omega}$-derivative of Eq. (19) vanish at the points $\boldsymbol{\Lambda}_m$ $(m=1,\ldots,n-1)$.

3.2.2 Complex potential of a unit body circulation

The complex potential of a unit body circulation is obtained in the $\boldsymbol{\omega}$-plane by requiring that the resulting conjugate velocity in the $\boldsymbol{x}$-plane: 1) asymptotically tend to $1/(2\pi\boldsymbol{i}\,\boldsymbol{x})$ for $\boldsymbol{x}\to\infty$; 2) be tangent to the body boundary; and 3) be regular at the critical points $\boldsymbol{Y}_m$.

From the remarks in Subsec. 3.2.1, the following complex potential is assumed:

$$\tilde{\boldsymbol{\Phi}}^{(b)}(\boldsymbol{\omega};t)= \frac{1}{2\pi\boldsymbol{i}}\log\boldsymbol{\omega}+\frac{1}{2\pi\boldsymbol{i}}\sum_{k=1}^{n-1}\left\{\log[\boldsymbol{\omega}-r_k(t)\,\boldsymbol{\sigma}_k(t)]+\log\boldsymbol{\omega}-\log[\boldsymbol{\omega}-\boldsymbol{\sigma}_k(t)/r_k(t)]\right\} \tag{20}$$

The first contribution is the complex potential of a unit body circulation around a flat plate [17]. Since the conjugate velocity in the $\boldsymbol{x}$-plane due to this term alone does not have the required asymptotic behavior for deformed airfoils ($n>1$ in Eq. (1)), further $n-1$ logarithmic contributions of the form $\log[\boldsymbol{\omega}-r_k(t)\boldsymbol{\sigma}_k(t)]$ are also present in Eq. (20). The singular points $r_k(t)\boldsymbol{\omega}_k(t)$ and the conjugates of their reciprocals must be located outside $D(t)$, which is verified with the choice $\boldsymbol{\sigma}_k(t):=\boldsymbol{\Lambda}_k(t)/\Lambda_k$ and $r_k>\Lambda_k$. The last two terms in the summation of Eq. (20) are obtained using the circle theorem [17] to satisfy no-penetration. The regularity of the velocity field due to Eq. (20) at the critical points $\boldsymbol{Y}_m$ is satisfied by evaluating the distances r_k so that the $\boldsymbol{\omega}$-derivative of Eq. (20) vanish at the points $\boldsymbol{\Lambda}_m$.

3.2.3 Complex potential of the circulatory flow

Using Eq. (19) and (20), the circulatory terms in Eq. (8) are written as

$$\tilde{\boldsymbol{\Phi}}^{(c)}(\boldsymbol{\omega};t)=\sum_{j=1}^{N(t)}\Gamma_j\,\tilde{\boldsymbol{\Phi}}_j^{(v)}(\boldsymbol{\omega};t)+\Gamma_b(t)\,\tilde{\boldsymbol{\Phi}}^{(b)}(\boldsymbol{\omega};t) \tag{21}$$

where N is the total number of discrete vortices shed into the wake, Γ_j is the time-constant circulation of the jth point vortex, and $\Gamma_b(t)$ is the instantaneous circulation around the body given by Kelvin theorem.

Vortex shedding is modeled using the fixed-position method [19]. The initial position of the nascent vortex, namely the Nth vortex in Eq. (21), is assumed in the $\boldsymbol{\omega}$-plane as $\boldsymbol{\omega}_{v_N}:=1+\delta$,

with $0 < \delta \ll 1$ assigned such that the vortex is introduced in the $\boldsymbol{x}$-plane close to the airfoil trailing edge. The circulation of the nascent vortex Γ_N is obtained by imposing that the total conjugate velocity in the $\boldsymbol{\omega}$-plane vanish at the point $\boldsymbol{\omega} = +1$, so removing the trailing-edge singularity of the conjugate velocity in the $\boldsymbol{x}$-plane [Eq. (6)]:

$$\partial_{\boldsymbol{\omega}} \tilde{\boldsymbol{\Phi}}^{(nc)} \Big|_{\boldsymbol{\omega} = +1} + \partial_{\boldsymbol{\omega}} \tilde{\boldsymbol{\Phi}}^{(c)} \Big|_{\boldsymbol{\omega} = +1} + \Gamma_N \, \partial_{\boldsymbol{\omega}} \tilde{\boldsymbol{\Phi}}_N^{(v)} \Big|_{\boldsymbol{\omega} = +1} = 0 \tag{22}$$

In the above equation, the complex potential of the circulatory flow (second term) include the $N - 1$ contributions due to the vortices already shed into the wake and the term due to the consequent body circulation, whereas the contribution due to the nascent vortex is considered separately (third term).

Once shed, each vortex is convected downstream with the local velocity

$$\dot{\boldsymbol{x}}_{v_j}(t) = \overline{\partial_{\boldsymbol{\omega}} \tilde{\boldsymbol{\Phi}}(\boldsymbol{\omega}; t) / \partial_{\boldsymbol{\omega}} \boldsymbol{x}(\boldsymbol{\omega}; t)} \Big|_{\boldsymbol{\omega} = \boldsymbol{\omega}_{v_j}(t)} \tag{23}$$

in order to allow free wake dynamics. For numerical simulation, Eq. (23) is evaluated by regularizing the Biot-Savart kernel as discussed in Ref. [20].

3.3 Velocity jumps across the branch cuts

In Subsec. 2.3 it has been observed that the velocity field given by Eq. (6) with complex potential given by Eq. (8) has jump discontinuities across the branch cuts of the map located in the fluid domain. Indeed, the jump of the conjugate velocity [Eq. (6)] at a generic point $\boldsymbol{x}^{\pm} = \boldsymbol{x}(\boldsymbol{\omega}^{\pm}) \in \mathcal{BC}_k$ $(k = 1, \ldots, n-1)$ is evaluated as follows:

$$\overline{\boldsymbol{u}}[\boldsymbol{x}(\boldsymbol{\omega}^+; t); t] - \overline{\boldsymbol{u}}[\boldsymbol{x}(\boldsymbol{\omega}^-; t); t] = \frac{1}{\partial_{\boldsymbol{\omega}} \boldsymbol{x}(\boldsymbol{\omega}^+; t)} \left[\partial_{\boldsymbol{\omega}} \tilde{\boldsymbol{\Phi}}(\boldsymbol{\omega}^+; t) + \partial_{\boldsymbol{\omega}} \tilde{\boldsymbol{\Phi}}(\boldsymbol{\omega}^-; t) \right] \tag{24}$$

where the relation $\partial_{\boldsymbol{\omega}} \boldsymbol{x}(\boldsymbol{\omega}^+; t) = -\partial_{\boldsymbol{\omega}} \boldsymbol{x}(\boldsymbol{\omega}^-; t)$ valid on $\mathcal{BCP}_k$ has been used. The quantity in Eq. (24) vanishes at the point $\boldsymbol{Y}_k$ due to the imposed regularity conditions and at infinity due to the recovery of the freestream velocity (see Subsec. 3.1 and 3.2). However, it is non zero at other points on $\mathcal{BCP}_k$. This behavior has been motivated in Subsec. 2.3.

The distance between the curves $\mathcal{BC}_k$ and the airfoil increase for smaller body curvature, as expected since the map in Eq. (1) does not have branch cuts in the fluid domain in the flat-plate case (see Subsec. 2.2). Since the quantity in Eq. (24) tends to zero at infinity, velocity jumps across the branch cuts are thus expected to be small for moderate body deformation. In this condition, the velocity field can be reasonably described by the complex potential in Eq. (8), whereas a corrective term is needed for very large body deflections. This statement is supported with an example for the case of a curved airfoil described by Eq. (1) for $n = 2$ and immersed in a fluid at rest ($\boldsymbol{u}_\infty = 0$). The airfoil is also at rest with no circulation around its boundary. A vortex of unit circulation is placed in the fluid domain at $\boldsymbol{x}_v = -1 + \boldsymbol{i}0.5$. The vortex-induced velocity field is analytically obtained from Eq. (6) with complex potential given by Eq. (19) and it is compared with a numerical solution from a panel code. The latter assumes the body boundary in Eq. (2) as camberline but introduces a finite thickness $\delta_t \ll \ell$ and rounded edges. The analytical and numerical velocity fields for two increasingly deformed body shapes are compared in Figs. 7 and 8. Figure 7 shows a good agreement since the velocity jump across the branch cut (red curve) given by the theoretical model is very slight for the moderately

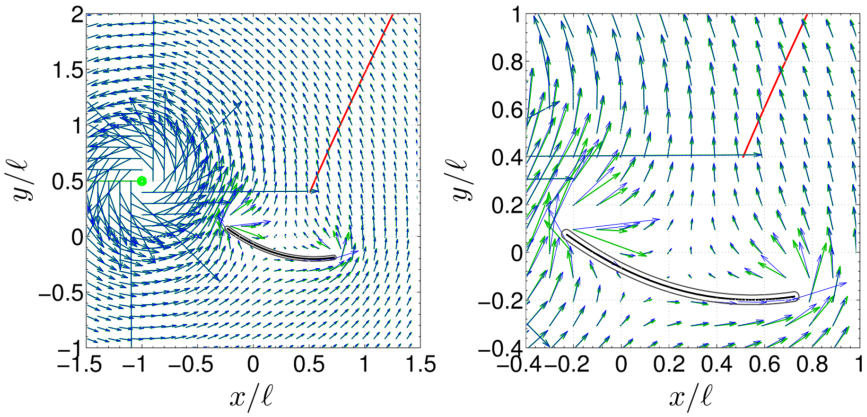

Figure 7: Analytical (green) and numerical (blue) velocity fields due to a unit-circulation point vortex at the point $\boldsymbol{x}_v = -1 + \boldsymbol{i}0.5$ outside a curved airfoil with mean camberline modeled by Eq. (1) for $n = 2$, $\ell = 1$, $\boldsymbol{h} = 0.25 - \boldsymbol{i}0.1$, $\alpha = 15°$, $\boldsymbol{c}_1 = 1$,$\boldsymbol{c}_2 = -0.02 + \boldsymbol{i}0.1$.

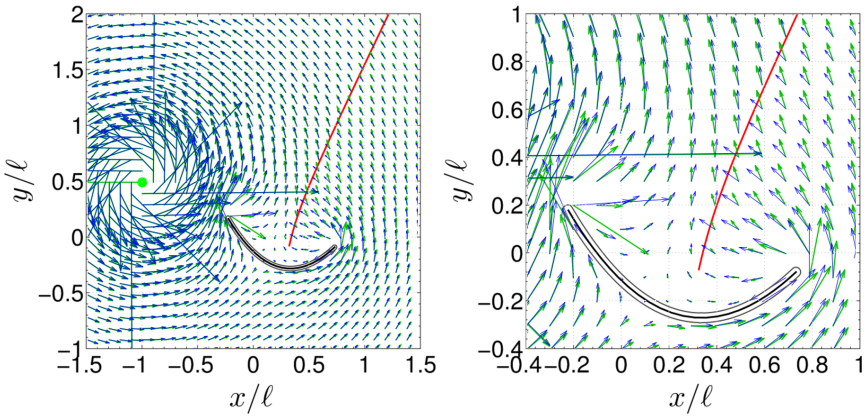

Figure 8: Analytical (green) and numerical (blue) velocity fields due to a unit-circulation point vortex at the point $\boldsymbol{x}_v = -1 + \boldsymbol{i}0.5$ outside a curved airfoil with mean camberline modeled by Eq. (1) for $n = 2$, $\ell = 1$, $\boldsymbol{h} = 0.25 - \boldsymbol{i}0.1$, $\alpha = 15°$, $\boldsymbol{c}_1 = 1$,$\boldsymbol{c}_2 = -0.06 + \boldsymbol{i}0.3$.

curved geometry. Minor differences around the airfoil edges are expected since the panel code considers a finite body thickness. Conversely, the numerical and analytical solutions show more appreciable differences in Fig. 8 since the theoretical model gives a significant velocity jump across the branch cut for very large curvatures.

The examples in Figs. 7 and 8 show that for deformations of aeronautical interest the complex potential in Eq. (19) can be used to describe the velocity field around a flexible thin airfoil, whereas a corrective term to remove velocity jumps in the fluid domain is necessary for applications involving very large curvatures (*e.g.,* fish locomotion). The methodology to correct sectional-analytical functions to remove jump discontinuities across curves is well established and based on the use of Cauchy integrals [18]. The standard corrective term shall be adapted to the present case by imposing that it also gives tangent velocity on the airfoil boundary. The development of such correction is beyond the scope of this paper and will be addressed in future works. In the following discussion it is assumed that the body curvature is such that velocity jumps across the branch cuts of the map [Eq. (1)] in the fluid domain can be neglected.

4 PRESSURE JUMP EVALUATION

The pressure jump distribution on the airfoil is obtained analytically using Bernoulli theorem, the map in Eq. (1), and the complex potential in Eq. (8). The following result is also valid in case a corrective complex potential is added to Eq. (8) to remove the velocity jumps across the branch cuts of the map in Eq. (1) in the fluid domain.

The jump of a generic complex function on the airfoil boundary is introduced as

$$[\boldsymbol{f}](\theta;t) := \boldsymbol{f}(e^{\boldsymbol{i}\theta^+};t) - \boldsymbol{f}(e^{\boldsymbol{i}\theta^-};t)$$

with $\theta^+ := \theta \in [0;\pi]$ (upper side) and $\theta^- := 2\pi - \theta^+$ (lower side). Hence, using Bernoulli theorem one has $[p]/\rho = -\left([\partial_t\varphi] + [|\boldsymbol{u}|^2]/2\right)$, where p is pressure, ρ is the constant fluid density, and φ is the velocity potential given by the real part of the complex potential $\boldsymbol{\Phi}$ [17]. The first contribution to the pressure jump is evaluated by rewriting the time derivative of $\boldsymbol{\Phi}$ in terms of derivatives of $\tilde{\boldsymbol{\Phi}}$ as follows:

$$\partial_t\boldsymbol{\Phi} = \partial_t\tilde{\boldsymbol{\Phi}} + \partial_{\boldsymbol{\omega}}\tilde{\boldsymbol{\Phi}}\,\partial_t\boldsymbol{\zeta} = \partial_t\tilde{\boldsymbol{\Phi}} - \partial_{\boldsymbol{\omega}}\tilde{\boldsymbol{\Phi}}\,\frac{\partial_t\boldsymbol{x}}{\partial_{\boldsymbol{\omega}}\boldsymbol{x}} = \partial_t\tilde{\boldsymbol{\Phi}} - \overline{\boldsymbol{u}}\,\partial_t\boldsymbol{x}$$

where the relation $\partial_t\boldsymbol{\omega} = -\partial_t\boldsymbol{x}/\partial_{\boldsymbol{\omega}}\boldsymbol{x}$ and Eq. (6) have been used. Noting that $\partial_t\boldsymbol{x} =: \boldsymbol{u}_b$ [Eq. (3)] achieves equal values at corresponding points on the airfoil upper and lower sides, the pressure jump divided by ρ becomes

$$\frac{[p]}{\rho} = -\frac{1}{2}\left\{\,\partial_t([\tilde{\boldsymbol{\Phi}}] + [\overline{\tilde{\boldsymbol{\Phi}}}]) - [\overline{\boldsymbol{u}}]\,\boldsymbol{u}_b - [\boldsymbol{u}]\,\overline{\boldsymbol{u}}_b + [\boldsymbol{u}\,\overline{\boldsymbol{u}}]\,\right\}$$

The time-derivative contributions on the right-hand side are linear, so that a separation of noncirculatory and circulatory effects is possible. The other terms on the right-hand side of Eq. (25) are nonlinear and involve products between the derivatives of noncirculatory and circulatory contributions in Eq. (8) and products of these derivatives and the velocity of the body boundary in Eq. (3).

5 NUMERICAL RESULTS

The capabilities of the present model are demonstrated by means of an application. The general formulation developed in Secs. 2 and 3 is specialized to the case $n = 2$ and implemented to simulate a cantilevered flexible airfoil undergoing imposed motion in a steady axial flow. Assuming $n = 2$ in Eq. (1), this reduces to

$$\boldsymbol{x}(\boldsymbol{\omega};t) = \boldsymbol{h}(t) + \frac{\ell\,\overline{\boldsymbol{\chi}}(t)}{4}\left[\,\boldsymbol{c}_1(t)\,\left(\,\boldsymbol{\omega} + \frac{1}{\boldsymbol{\omega}}\,\right) + \boldsymbol{c}_2(t)\,\left(\,\boldsymbol{\omega}^2 + \frac{1}{\boldsymbol{\omega}^2}\,\right)\,\right] \tag{25}$$

with Laurent coefficients $\boldsymbol{c}_1(t) = m_1(t)\exp[\boldsymbol{i}\varphi_1(t)]$ and $\boldsymbol{c}_2(t) = m_2(t)\exp[\boldsymbol{i}\varphi_2(t)]$. The map in Eq. (25) describes a flexible thin airfoil that for any time shows curvature of constant sign along the chord. The presence of the second-order powers of $\boldsymbol{\omega}$ and $1/\boldsymbol{\omega}$ in Eq. (25) implies that the map has one branch cut $\mathcal{BC}_1$ inside the flow field with origin at the critical point $\boldsymbol{Y}_1$. An imposed motion for the airfoil modeled by Eq. (25) is obtained in Sec. 5.1 by assuming clamped boundary conditions at the leading edge and by requiring that the body length be conserved. Pressure jump distributions on the body and free wake configurations at different times during the motion are presented in Sec. 5.2.

5.1 Imposed motion

The airfoil modeled using Eq. (25) is assumed to be cantilevered at the leading-edge and horizontal in its undeformed configuration ($\boldsymbol{\chi} = 1$). With this choice and imposing that the leading edge is at the origin of the $\boldsymbol{x}$-plane, Eq. (25) gives

$$\boldsymbol{h} = \frac{\ell}{2}\,(\boldsymbol{c}_1 - \boldsymbol{c}_2) \tag{26}$$

Assuming the angle $\theta \in (-\pi, +\pi]$ as parameter for the body boundary, the local tangent unit vector is

$$\boldsymbol{\tau}(\theta; t) = \mp \frac{\boldsymbol{c}_1(t) + 4\boldsymbol{c}_2(t)\cos\theta}{|\boldsymbol{c}_1(t) + 4\boldsymbol{c}_2(t)\cos\theta|}$$

where the minus sign is used for $0 \leq \theta \leq \pi$ (upper side) and the plus sign for $-\pi < \theta \leq 0$ (lower side). Due to the assumed boundary conditions, the tangent vector must be in the negative direction of the horizontal axis at the leading edge, namely $\boldsymbol{\tau}(\pi; t) \equiv -1$. Therefore, the Laurent coefficient verify the following constraint:

$$\boldsymbol{c}_1(t) - 4\boldsymbol{c}_2(t) = \gamma(t) \tag{27}$$

where $\gamma > 0$ is a real quantity. Using Eq. (25), the conservation of the body length is written as

$$\ell = \int_0^\pi d\theta\; |\partial_\theta \boldsymbol{x}| = \frac{\ell}{2}\int_0^\pi d\theta\; \sin\theta\; \left[\, m_1^2 + 8m_1 m_2 \cos(\varphi_1 - \varphi_2)\cos\theta + 16 m_2^2 \cos^2\theta \,\right]^{1/2}$$

This integral is conveniently evaluated by introducing the variable $\xi = \cos\theta$. With some manipulation, the result is recast as a nonlinear equation of the form $f(\gamma, c_2, \varphi_2) = 0$. This is solved via the Newton-Raphson method by assigning $\boldsymbol{c}_2(t) = m_2(t)\exp[\boldsymbol{i}\varphi_2(t)]$ to obtain $\gamma(t)$. The functions $\boldsymbol{c}_1(t)$ and $\boldsymbol{h}(t)$ are next evaluated using Eqs. (27) and (26). The imposed motion of the body boundary is finally obtained by substituting the functions $\boldsymbol{h}(t)$, $\boldsymbol{c}_1(t)$, and $\boldsymbol{c}_2(t)$ into the map in Eq. (25) evaluated for $\boldsymbol{\omega} \in \mathcal{C}$.

5.2 Case study

A motion obtained as in Sec. 5.1 is imposed to a flexible thin airfoil cantilevered at the leading edge. The body has undeformed length $\ell = 1$ m and it is immersed in a steady flow of freestream velocity $\boldsymbol{u}_\infty = 1$ m/s. The time history of $\boldsymbol{c}_2(t)$ is assigned in terms of its modulus $m_2(t) = m_{2_0} + \Delta m_2 \cos(2\pi t/T_m)$ and phase $\varphi_2(t) = \varphi_{2_0} + \Delta\varphi_2 \sin(2\pi t/T_\varphi)$, with $m_{2_0} = 0.03$, $\Delta m_2 = 0.02$, $\varphi_{2_0} = 0^\circ$, $\Delta\varphi_2 = 20^\circ$, and $T_m = T_\varphi = 1$ s. The time histories of $\boldsymbol{c}_1$ and $\boldsymbol{h}$ are obtained as in Subsec. 5.1 in order to conserve the body length during the oscillation. The true-scale airfoil deformed configurations are shown at different times over a period in Fig. 9. The body deflection over chord is up to 5%.

The unsteady aerodynamics around the flexible thin airfoil due to its imposed motion is simulated by integrating the free wake dynamics via a fourth-order Runge-Kutta time marching algorithm. Details on the numerical procedure are provided in Ref. [16]. The unsteady pressure jump distribution along the chord is evaluated analytically at any time using Eq. (25). The noncirculatory effects, body-circulation effects, and wake effects are separated in the linear time-derivative term, whereas the quadratic terms are considered together. The distribution of the total pressure difference coefficient defined as $C_p = -2[p]/(\rho u_\infty^2)$ and of its separate

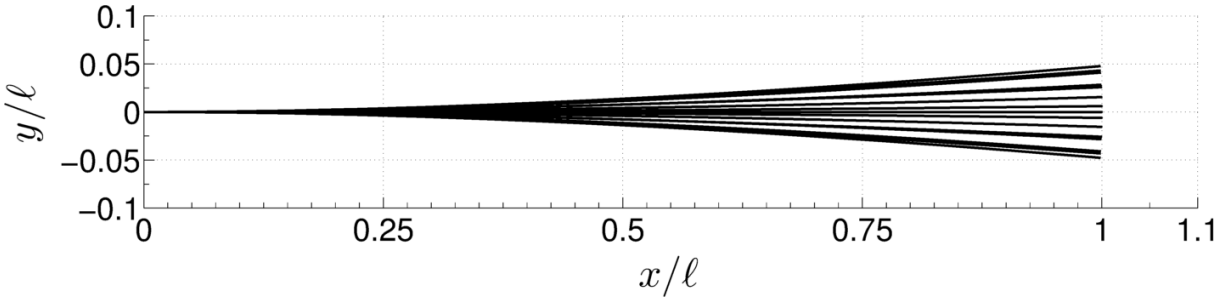

Figure 9: Cantilevered flexible thin airfoil undergoing imposed motion in a steady axial flow: true-scale deformed configuration at $t = jT_m/16$ s ($j = 0, 1, \ldots, 16$) for $\ell = 1$ m, $\boldsymbol{\chi} \equiv 1$, $T_m = 1$ s, and $\boldsymbol{c}_2(t) = [0.03 + 0.02\cos(2\pi t/T_m)]\exp\{\boldsymbol{i}[(\pi/9)\sin(2\pi t/T_m)]\}$ in Eq. (25) under the condition of constant body length.

contributions at different times during the third complete oscillation of the airfoil and the corresponding wake geometries are illustrated in Figs. 10 and 11. The plots on the left-hand side shows that the quadratic contributions and the time-derivative contribution due to the wake in the total pressure difference coefficient [Eq. (25)] remain small along the chord compared to the time-derivative contributions due to noncirculatory effects and to the body circulation. As a consequence, the total pressure difference coefficient is approximatively given by the sum of the latter terms. The time-derivative term due to noncirculatory effects increase during the ascending and descending phases, as expected due to the consequent increase in modulus of the body boundary acceleration (see Figs. 10(a), 10(c), 11(c), and 11(e)). Conversely, they are small when the airfoil is in horizontal configuration (see Figs. 10(e), 10(g), 11(a), and 11(g)). The time-derivative terms due to the body circulation is larger when the vorticity shed into the wake experiences a sign change, which results in the generation of a new macroscopic vortex structure (see Figs. 10(c), 10(e), 11(a), 11(e), and 11(g)). The wake configurations in the plots on the right-hand side of Fig. 11 show a starting vortex due to the zero initial circulation around the body. Since the vorticity shed into the wake changes sign during the airfoil oscillation, the wake organizes in dipoles due to the rotation of vortices having circulation of opposite sign about each other. The dipoles are convected downstream approximatively with the velocity of the undisturbed flow and do not show a significant global rotation about any of the two poles, so showing that the total vorticity content associated with each pole is about equal in modulus.

6 CONCLUDING REMARKS

A semi-analytical formulation for the unsteady aerodynamics of flat plates has been extended to flexible thin airfoils. The velocity field has been described by means of a complex potential, which has been evaluated by mapping the airfoil boundary onto a circle. This well-established approach traditionally adopted in several small disturbance theories has been generalized to airfoil rigid-body motion and deformation of arbitrary amplitude, under the only assumptions of attached flow and constant body length. Non-planar wake has been taken into account using a discrete-vortex method to model vorticity shedding from the airfoil trailing edge. A semi-analytical solution for the unsteady pressure jump on the body has been obtained that simultaneously takes into account large-amplitude rigid-body motion, body flexibility, and free wake. This result may be used for parametric studies and as complex benchmark for assessment of high-order fully numerical models. The limits of the proposed model for very large body deformation have been discussed by comparing two vortex-induced velocity fields with a numerical solution from a panel code. It has been shown that the model well describes the velocity field

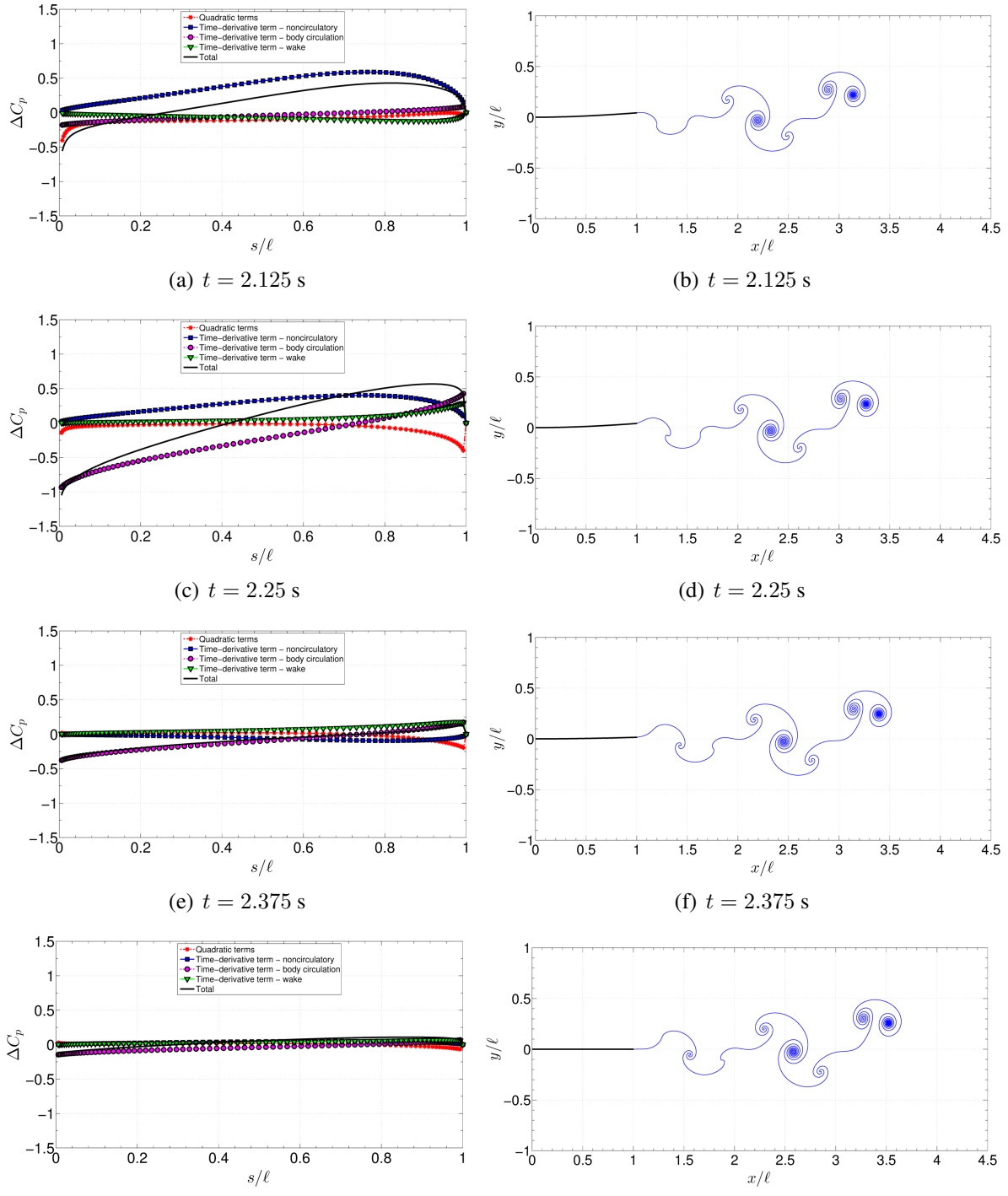

(a) $t = 2.125$ s (b) $t = 2.125$ s

(c) $t = 2.25$ s (d) $t = 2.25$ s

(e) $t = 2.375$ s (f) $t = 2.375$ s

(g) $t = 2.5$ s (h) $t = 2.5$ s

Figure 10: Cantilevered flexible thin airfoil undergoing imposed motion in a steady axial flow: pressure difference coefficient and wake configuration at $t = 2 + j\,T_m/8$ s ($j = 1, 2, 3, 4$) for $\ell = 1$ m, $\boldsymbol{\chi} \equiv 1$, $\boldsymbol{c}_2(t) = [0.02{+}0.03\cos(2\pi t/T_m)]\exp\{\boldsymbol{i}[(\pi/9)\sin(2\pi t/T_m)]\}$ in Eq. (25) under the condition of constant body length.

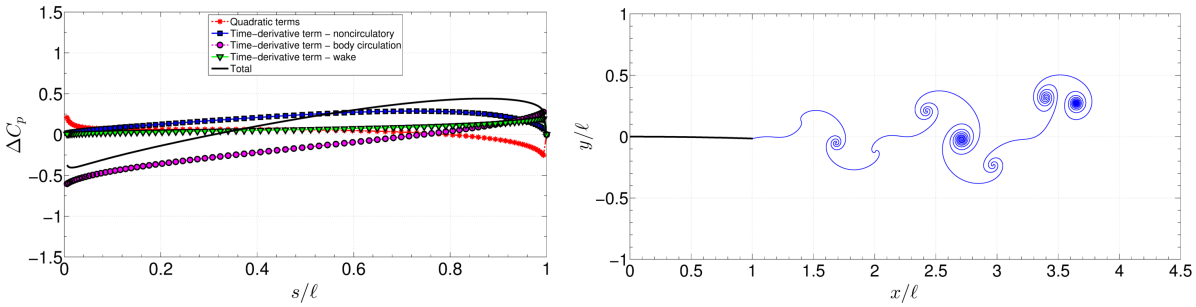

(a) $t = 2.625$ s (b) $t = 2.625$ s

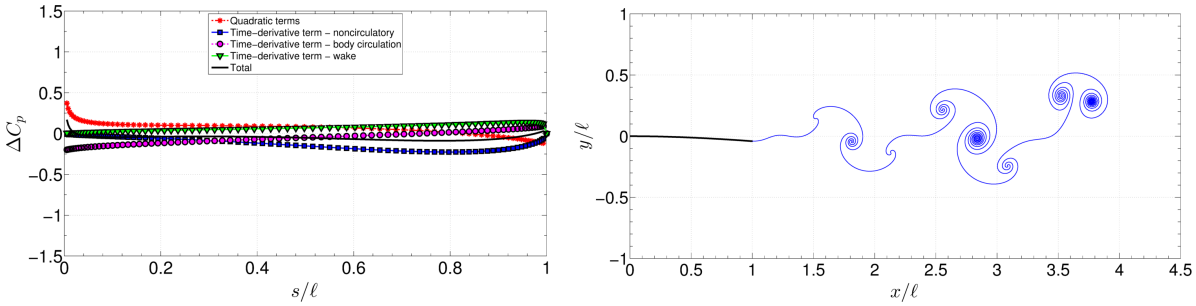

(c) $t = 2.75$ s (d) $t = 2.75$ s

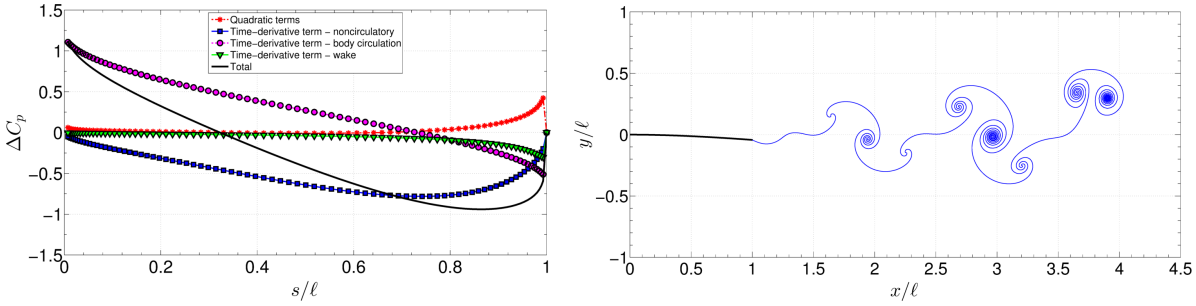

(e) $t = 2.875$ s (f) $t = 2.875$ s

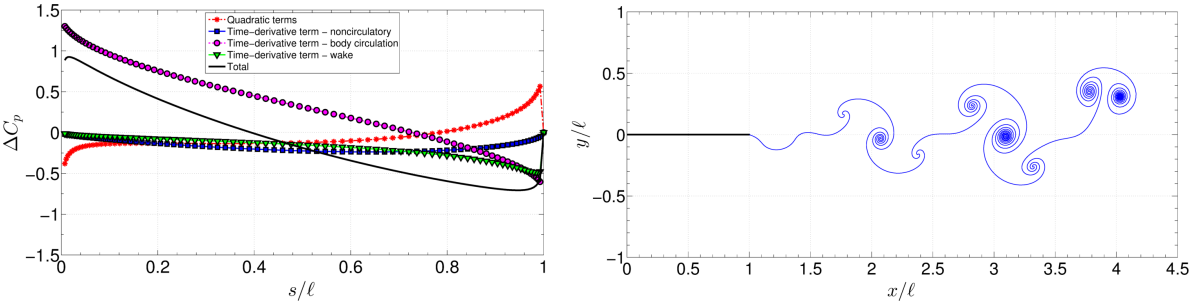

(g) $t = 3$ s (h) $t = 3$ s

Figure 11: Cantilevered flexible thin airfoil undergoing imposed motion in a steady axial flow: pressure difference coefficient and wake configuration at $t = 2 + j\,T_m/8$ s ($j = 5, 6, 7, 8$) for $\ell = 1$ m, $\boldsymbol{\chi} \equiv 1$, $\boldsymbol{c}_2(t) = [0.03{+}0.02\cos(2\pi t/T_m)]\exp\{\boldsymbol{i}[(\pi/9)\sin(2\pi t/T_m)]\}$ in Eq. (25) under the condition of constant body length.

for airfoil curvatures of aeronautical interest, while a methodology to further improve the prediction for very large deformations has been outlined. To demonstrate the applicability of the present formulation to practical fluid-structure interaction problems, the model has been implemented to to simulate a cantilevered flexible airfoil undergoing imposed motion in a steady axial flow. Numerical results for the unsteady pressure jump on the body and free wake configurations have been discussed. Future work will address comparison of the theoretical model with experimental results and its integration with a consistent structural model to perform aeroelastic simulations of flexible thin airfoils in arbitrary motion.

ACKNOWLEDGMENTS

This paper has been supported by the Sapienza University of Rome project "Reduced Order Models (ROM) for Fluid-Structure Interactions".

7 REFERENCES

[1] Wagner, H., "Über die Entstehung des Dynamischen Auftriebes von Tragflügeln", *ZAMM*, Vol. 5, No. 1, 1925, pp. 17–35.

[2] Küssner, H. G., "Zusammenfassender Bericht über den instationren Auftrieb von Flügeln", *Luftfahrtforschung*, Vol. 13, No. 12, 1936, pp. 410–424.

[3] Theodorsen, T., "General Theory of Aerodynamic Instability and the Mechanism of Flutter,"NACA TR No. 496, 1935.

[4] Isaacs, R., "Airfoil Theory for Rotary Wing Aircraft", *Journal of the Aeronautical Sciences*, Vol. 12, No. 1, 1945, pp. 113–117.

[5] Bisplinghoff, R. L., Ashley, H., and Halfman, R. L., *Aeroelasticity*, Dover Publications, Mineola, NY, 1996.

[6] Peters, D. A., Karunamoorthy, S., and Cao, W., "Finite State Induced Flow Models. Part I: Two-Dimensional Thin Airfoil", *Journal of Aircraft*, Vol. 32, No. 2, 1995, pp. 313–322.

[7] Peters, D. A., and Hsieh, M. A., "A State-space Airloads Theory for Flexible Airfoils", *Journal of American Helicopter Society*, Vol. 52, No. 4, 2007, pp. 329–342.

[8] Walker, W. P., and Patil, M. J., "Unsteady Aerodynamics of Deformable Thin Airfoils", *Journal of Aircraft*, Vol. 52, No. 6, 2014, pp. 1673–1680.

[9] Li, D., Wu, Y., Da Ronch, A., and Xiang, J., "Energy Harvesting by means of Flow-Induced Vibrations on Aerospace Vehicles", *Progress in Aerospace Sciences*, Vol. 86, 2016, pp. 28–62.

[10] Liu, H., Ravi, S., Kolomenskiy, D., and Tanaka, H. "Biomechanics and Biomimetics in Insect-Inspired Flight Systems", *Philosophical Transactions of the Royal Society B: Biological Sciences*, Vol. 371, No. 1704, 2016, pp. 1–12.

[11] Ward, T.A., Rezadad, M., Fearday, C.J., and Viyapuri, R., "A Review of Biomimetic Air Vehicle Research: 1984-2014", *International Journal of Micro Air Vehicles* Vol. 7, No. 3, 2015, pp. 375-394.

[12] Ramesh, K., Gopalarathnam, A., Edwards, J. R., Ol, M. V., and Granlund, K., "An Unsteady Airfoil Theory Applied to Pitching Motions Validated Against Experiment and Computation", *Theoretical Computational Fluid Dynamics*, Vol. 27, 2013, pp. 843–864.

[13] Xia, X., Mohseni, K., "Lift Evaluation of a Two-dimensional Pitching Flat Plate", *Physics of Fluids*, Vol. 25, No. 091901, 2013, pp. 1–26.

[14] Wang, C., and Eldredge, J. D., "Low-Order Phenomenological Modeling of Leading-Edge Vortex Formation", *Theoretical Computational Fluid Dynamics*, Vol. 27, 2013, pp. 577–598.

[15] Yan, Z., Taha, H. E., and Hajj, M. R., "Geometrically-Exact Unsteady Model for Airfoils Undergoing Large", *Aerospace Science and Technology*, Vol. 39, 2014, pp. 293–306.

[16] Riso, C., Riccardi, G., Mastroddi, F., "Nonlinear Aeroelastic Modeling via Conformal Mapping and Vortex Method for a Flat-Plate Airfoil in Arbitrary Motion", *Journal of Fluids and Structures*, Vol. 62, 2016, pp. 230–251.

[17] Milne-Thomson, L. M., *Theoretical Hydrodynamics*, Dover Publications, Mineola, NY, 1996.

[18] Ablowitz, M. J., and Fokas, A. S., *Complex Variables: Introduction and Applications*, Cambridge University Press, Cambridge, England, UK, 2003.

[19] Kiya, M., and Arie, M., "A Contribution to an Inviscid Vortex-Shedding Model for an Inclined Flat Plate in Uniform Flow", *Journal of Fluid Mechanics*, Vol. 82, No. 2, 1977, pp. 223-240.

[20] Majda, A. J., and Bertozzi, A. L., *Vorticity and Incompressible Flow*, Cambridge University Press, Cambridge, England, UK, 2002 .

COPYRIGHT STATEMENT